Hindawi
Mathematical Problems in Engineering
Volume 2019, Article ID 3980181, 6 pages
https://doi.org/10.1155/2019/3980181

Research Article

Image Segmentation Based on Modified Fractional Allen–Cahn Equation

Dongsun Lee[1] **and Seunggyu Lee**[2]

[1]*Department of Mathematical Sciences, Ulsan National Institute of Science and Technology, Ulsan 689-798, Republic of Korea*
[2]*National Institute for Mathematical Sciences, Daejeon 34047, Republic of Korea*

Correspondence should be addressed to Seunggyu Lee; sglee89@nims.re.kr

Received 31 October 2018; Accepted 14 January 2019; Published 30 January 2019

Academic Editor: John D. Clayton

We present the image segmentation model using the modified Allen–Cahn equation with a fractional Laplacian. The motion of the interface for the classical Allen–Cahn equation is known as the mean curvature flows, whereas its dynamics is changed to the macroscopic limit of Lévy process by replacing the Laplacian operator with the fractional one. To numerical implementation, we prove the unconditionally unique solvability and energy stability of the numerical scheme for the proposed model. The effect of a fractional Laplacian operator in our own and in the Allen–Cahn equation is checked by numerical simulations. Finally, we give some image segmentation results with different fractional order, including the standard Laplacian operator.

1. Introduction

Image segmentation is a process of image partitioning into nonintersection parts with similar properties such as gray level, color, texture, brightness, and contrast [1]. The medical image segmentation is important to study anatomical structures, to identify region of interest such as tumor, lesion, and other abnormalities, to measure tissue volume of tumor or area of lesion, and to help in treatment planning [2].

One of the most widely used methods for image segmentation is the Mumford–Shah model [3] and it has been extensively studied and extended in many works [4–6].

This paper is organized as follows: In Section 2, we describe the mathematical model for the image segmentation using a fractional Laplacian operator. In Section 3, simulation results are shown for effect of a fractional operator and image segmentations. Finally, the conclusion is drawn in Section 4.

2. Mathematical Model

2.1. Fractional Allen–Cahn Equation. The Allen–Cahn equation, which was first introduced to describe coarsening in binary alloys [7], is a gradient flow under L^2-inner product space with the following Ginzburg–Landau free energy functional:

$$\mathscr{E}^{AC}(\phi) = \int_\Omega \left(\frac{F(\phi)}{\epsilon^2} + \frac{1}{2}\left|\nabla\phi\right|^2 \right) d\mathbf{x}, \tag{1}$$

and it has the following form:

$$\frac{\partial\phi(\mathbf{x},t)}{\partial t} = -\text{grad}\mathscr{E}^{AC}(\phi) = -\frac{F'(\phi)}{\epsilon^2} + \Delta\phi. \tag{2}$$

Here $\phi(\mathbf{x},t) \in [-1,1]$ is the concentration defined in a bounded domain $\Omega \in \mathbb{R}^2$, ϵ is the coefficient related to an interfacial energy, and $F(\phi) = 0.25(1-\phi^2)^2$ is the double-well potential energy function.

In recent years, the fractional Allen–Cahn equation has been researched in some literature to study the competing stable phases having an identical Lyapunov functional density [8–10]:

$$\frac{\partial\phi}{\partial t} = -\frac{F'(\phi)}{\epsilon^2} + \Delta_{\mathbf{x}}^s\phi, \tag{3}$$

where $\Delta_{\mathbf{x}}^s$ is the fractional Laplacian, obtained as the macroscopic limit of Lévy process [11], with fractional order $0 <$

$s \leq 1$. Here, the macroscopic limit in space is computed by considering that the microscopic spatial scale is very small. Indeed, when the random walk involves correlations, non-Gaussian or non-Markovian memory effects, the classical diffusion equation fails to describe the macroscopic limit. However a generalization of the Brownian random walk (Lévy process) model allows us to have the incorporation of nondiffusive effects. It eventually leads to the fractional Laplacian instead of the classical Laplacian in the macroscopic limit. Note that similar models have been studied in physical literature in a very different context such as a barrier crossing of a particle driven by white symmetric Lévy noise [12–16].

2.2. Modification to Image Segmentation. Let $f_0(\mathbf{x}) : \Omega \longrightarrow [0,1]$ be a grayscale given image. Then, the Mumford–Shah model, which is one of the most widely used models for image segmentation [3], minimizes the following functional to perform image segmentation:

$$\mathscr{E}^{MS}(u,C) = \nu_1 \text{Length}(C) + \nu_2 \int_\Omega |f_0 - u|^2 \, d\mathbf{x} + \nu_3 \int_{\Omega - C} |\nabla u|^2 \, d\mathbf{x}, \tag{4}$$

where u is the piecewise smooth function approximating f_0, C is the segmenting curve representing the set of edges in the given image u, and ν_1, ν_2, ν_3 are the positive constants. Let us modify the energy functional (4) as a phase-field formulation. First, it should be noted that C can be considered as the zero-contour of ϕ. Then, the following equation holds:

$$\text{Length}(C) = \int_C 1 d\mathbf{x} \approx \int_\Omega \frac{F(\phi)}{\epsilon^2} d\mathbf{x}. \tag{5}$$

Next, if we replace u with $(1+\phi)/2$, (4) can be written as follows:

$$\mathscr{E}^{MS}(\phi) = \nu_1 \int_\Omega \frac{F(\phi)}{\epsilon^2} d\mathbf{x} + \nu_2 \int_\Omega \left| f_0 - \frac{1+\phi}{2} \right|^2 d\mathbf{x} + \nu_3 \int_{\Omega - C} \left| \nabla \left(\frac{1+\phi}{2} \right) \right|^2 d\mathbf{x}. \tag{6}$$

Since $\nabla\phi = 0$ at $\mathbf{x} \in C$, $\int_\Omega |\nabla\phi|^2 d\mathbf{x} = \int_{\Omega - C} |\nabla\phi|^2 d\mathbf{x}$. Therefore, the fractional analogue phase-field approach of the Mumford–Shah model is considered as minimizing the following energy functional:

$$\mathscr{E}(\phi) = \int_\Omega \left(\frac{F(\phi)}{\epsilon^2} + \frac{1}{2} \left| (-\Delta)^{s/2} \phi \right|^2 \right) d\mathbf{x} + \mu \int_\Omega \left| f_0 - \frac{1+\phi}{2} \right|^2 d\mathbf{x}, \tag{7}$$

and the governing equation can be written as follows:

$$\frac{\partial \phi}{\partial t} = -\frac{\phi^3 - \phi}{\epsilon^2} + \Delta_{\mathbf{x}}^s \phi + \mu \left(f_0 - \frac{1+\phi}{2} \right). \tag{8}$$

2.3. Numerical Solution. We consider the Fourier spectral method in space and the linear convex splitting scheme, which is known as stable and uniquely solvable one [17], in time. First, the temporal discretization of (8) is written as follows:

$$\frac{\phi^{n+1} - \phi^n}{\Delta t} = -\frac{(\phi^n)^3 - 3\phi^n + 2\phi^{n+1}}{\epsilon^2} + \Delta_{\mathbf{x}}^s \phi^{n+1} + \mu \left(f_0 - \frac{1+\phi^{n+1}}{2} \right) \quad \text{for } n = 1, \ldots, n_t. \tag{9}$$

Remark that (9) has the bounded solution $\|\phi^n\|_\infty \leq 1$ for any $n = 1, \ldots, n_t$ if $\|f_0\|_\infty \leq 1$ and $\|\phi^0\|_\infty \leq 1$ where $\|\phi\|_\infty = \max_x \phi$ is the l^∞-norm. It comes from the fact that $-\Delta_{\mathbf{x}}^s$ has nonnegative eigenvalues.

Theorem 1. *The numerical scheme (9) is uniquely solvable for any time step $\Delta t > 0$.*

Proof. We consider following functional defined on a l^2-inner product space:

$$G(\phi) = \frac{1}{2} \|\phi\|_2^2 + \Delta t \mathscr{E}_c(\phi) - (S^n, \phi)_2, \tag{10}$$

where $(\phi, \psi)_2 = \int_\Omega \phi\psi d\mathbf{x}$ is the l^2-inner product, $\|\phi\|_2^2 = (\phi,\phi)_2$ is the l^2-norm, $\mathscr{E}_c(\phi) = (\phi^2/\epsilon^2, \mathbf{1})_2 + 0.5\|(-\Delta)_{\mathbf{x}}^{s/2}\phi\|_2^2 + \mu\|f_0 - 0.5(1+\phi)\|_2^2$, $S^n = \phi^n - \Delta t((\phi^n)^3 - 3\phi^n)/\epsilon^2$. Note that it can be solved if and only if G has the unique minimizer ϕ^{n+1}. For any ψ and scalar α,

$$\frac{d}{d\alpha} \mathscr{E}_c(\phi + \alpha\psi)\Big|_{\alpha=0} = \left(\frac{2\phi}{\epsilon^2} - \Delta_{\mathbf{x}}^s \phi - \mu \left(f_0 - \frac{1+\phi}{2} \right), \psi \right)_2, \tag{11}$$

$$\frac{d^2}{d\alpha^2} \mathscr{E}_c(\phi + \alpha\psi)\Big|_{\alpha=0} = \frac{2}{\epsilon^2} + \left\| (-\Delta)_{\mathbf{x}}^{s/2} \psi \right\|_2^2 + \frac{\mu}{2} \geq 0. \tag{12}$$

Therefore $\mathscr{E}_c(\phi)$ is convex, which implies that $G(\phi)$ is also convex. Note that the unique minimizer ϕ^{n+1} makes the first variation of $G(\phi)$ zeros, i.e.,

$$\left(\frac{\phi^{n+1} - \phi^n}{\Delta t} + \frac{(\phi^n)^3 - 3\phi^n + 2\phi^{n+1}}{\epsilon^2} - \Delta_{\mathbf{x}}^s \phi^{n+1} - \mu \left(f_0 - \frac{1+\phi^{n+1}}{2} \right), \psi \right)_2 = 0, \tag{13}$$

and it holds if and only if (9) holds. □

Theorem 2. *The numerical scheme (9) is unconditionally energy stable, i.e., $\mathscr{E}(\phi^{n+1}) \leq \mathscr{E}(\phi^n)$ for any time step $\Delta t > 0$.*

Proof. Note that we already prove that $\mathscr{E}_c(\phi)$ is convex in the proof of Theorem 1. Let $\mathscr{E}_e(\phi) = \mathscr{E}_c(\phi) - \mathscr{E}(\phi)$. Then, it is clear

that $\mathscr{E}_e(\phi)$ is concave since $\phi \in [-1,1]$ and the followings hold for any ϕ and ψ:

$$\begin{aligned}&\mathscr{E}_c(\phi) - \mathscr{E}_c(\psi)\\ &\le \left(\frac{2\phi}{\epsilon^2} - \Delta_{\mathbf{x}}^s\phi - \mu\left(f_0 - \frac{1+\phi}{2}\right), \phi - \psi\right)_2,\end{aligned} \tag{14}$$

$$\mathscr{E}_e(\phi) - \mathscr{E}_e(\psi) \ge \left(-\frac{\psi^3 - 3\psi}{\epsilon^2}, \phi - \psi\right)_2. \tag{15}$$

Then,

$$\begin{aligned}&\mathscr{E}(\phi) - \mathscr{E}(\psi) = (\mathscr{E}_c(\phi) - \mathscr{E}_c(\psi)) - (\mathscr{E}_e(\phi)\\ &- \mathscr{E}_e(\psi)) \le \left(\frac{2\phi}{\epsilon^2} - \Delta_{\mathbf{x}}^s\phi - \mu\left(f_0 - \frac{1+\phi}{2}\right)\right.\\ &\left. + \frac{\psi^3 - 3\psi}{\epsilon^2}, \phi - \psi\right)_2.\end{aligned} \tag{16}$$

We, respectively, replace ϕ and ψ with ϕ^{n+1} and ϕ^n. Then (9) says that

$$\begin{aligned}&\mathscr{E}\left(\phi^{n+1}\right) - \mathscr{E}\left(\phi^n\right) \le \left(\frac{\left(\phi^n\right)^3 - 3\phi^n + 2\phi^{n+1}}{\epsilon^2}\right.\\ &\left. - \Delta_{\mathbf{x}}^s\phi^{n+1} - \mu\left(f_0 - \frac{1+\phi^{n+1}}{2}\right), \phi^{n+1} - \phi^n\right)_2,\\ &= \left(-\frac{\phi^{n+1} - \phi}{\Delta t}, \phi^{n+1} - \phi\right)_2 = -\frac{1}{\Delta t}\left\|\phi^{n+1} - \phi\right\|_2^2\\ &\le 0.\end{aligned} \tag{17}$$

□

Before applying the Fourier spectral method, we present the Fourier definition of the fractional Laplacian operator.

Definition 3. The Fourier definition of $\Delta_{\mathbf{x}}^s$ is [19]

$$\mathscr{F}\left(\Delta_{\mathbf{x}}^s\phi\right)(\xi) = -|\xi|^s\,\mathscr{F}\phi(\xi), \tag{18}$$

where $\mathscr{F}(\cdot)$ is a Fourier transformation. Note that the Fourier transformation of the standard Laplacian operator is $\mathscr{F}(\Delta\phi)(\xi) = -|\xi|^2\mathscr{F}\phi(\xi)$.

By the definition, (9) can be written as follows using the discrete Fourier transformation $\mathscr{F}_h\phi^n \approx \sum_{p=-N_x/2}^{N_x/2-1}\sum_{q=-N_y/2}^{N_y/2-1}\widehat{\phi}_{pq}^n e^{2\pi(px/L_x+qy/L_y)}/(N_xN_y)$:

$$\begin{aligned}\frac{\widehat{\phi}_{pq}^{n+1} - \widehat{\phi}_{pq}^n}{\Delta t} &= -\frac{\left(\widehat{\phi}_{pq}^n\right)^3 - 3\widehat{\phi}_{pq}^n + 2\widehat{\phi}_{pq}^{n+1}}{\epsilon^2} - \left|\xi_{pq}\right|^s\widehat{\phi}_{pq}^{n+1}\\ &+ \mu\left(\widehat{f}_{0,pq} - \frac{1+\widehat{\phi}_{pq}^{n+1}}{2}\right),\end{aligned} \tag{19}$$

where $\widehat{\phi}$ is the discrete Fourier coefficient, L_x and L_y are, respectively, the length of the domain in x- and y-axis, N_x and N_y are, respectively, the number of grid points in x- and y–axis, Δt is the temporal step size, and $\xi_{pq}^2 = (2\pi p/L_x)^2 + (2\pi q/L_x)^2$. Therefore, we can get ϕ^{n+1} as follows:

$$\begin{aligned}\phi^{n+1} &\approx \mathscr{F}_h^1\widehat{\phi}_{pq}\\ &= \mathscr{F}_h^{-1}\left(\frac{\widehat{\phi}_{pq} + \Delta t\left(\left(3\widehat{\phi}_{pq} - \left(\widehat{\phi}_{pq}\right)^3\right)/\epsilon^2 + \mu\left(\widehat{f}_{0,pq} - 1/2\right)\right)}{1 + \Delta t\left(2/\epsilon^2 + \xi_{pq}^2 + \mu/2\right)}\right).\end{aligned} \tag{20}$$

3. Numerical Experiments

3.1. Effect of the Fractional Laplacian Operator. To observe the only difference between the fractional Laplacian $\Delta_{\mathbf{x}}^s$ and classical Laplacian $\Delta_{\mathbf{x}}$ in image segmentation, let us select $\epsilon \gg 1$ large enough such that

$$\frac{\phi^{n+1} - \phi^n}{\Delta t} \approx \widehat{\epsilon}\Delta_{\mathbf{x}}^s\phi^{n+1} + \mu\left(f_0 - \frac{1+\phi^{n+1}}{2}\right), \tag{21}$$

where $\widehat{\epsilon}$ is the rescaled parameter. Since scheme (9) has bounded and unconditionally stable solutions, it is easy to see that (21) has the same properties, as well. For the numerical illustration, we consider original and noise 512×512 images f_0^{true}, f_0^{noise}. We take the image f_0^{noise} as the initial data. The fractional orders and parameters for both operators $\Delta_{\mathbf{x}}^s$ and $\Delta_{\mathbf{x}}$ are given by $s = 0.5$, $\widehat{\epsilon} = 1.47$ and $s = 1$, $\widehat{\epsilon} = 0.01$, respectively. Note that there are no criteria of choosing the best parameters for image processing, while these parameters heuristically give the best result. The other parameters $\mu = 20$, $\Delta t = 0.0001$, $n_t = 40$ are used. For our convenience, we denote the final solution from the operator of fractional order s by $\widetilde{\phi}^s$.

With initial data f_0^{noise} and its error $\|f_0^{true} - f_0^{noise}\|_{fro} \approx 336.6$, we perform numerical tests. Comparisons are made for the numerical results which we have $\|f_0^{true} - \widetilde{\phi}^{0.5}\|_{fro} \approx \|f_0^{true} - \widetilde{\phi}^1\|_{fro} \approx 298.3$. If large noise is imposed upon the original image f_0^{true}, the value of $\|f_0^{true} - f_0^{noise}\|_{fro}$ is also large. If, the other way around, there is no noise, then f_0^{noise} is equal to f_0^{true}, i.e., $\|f_0^{true} - f_0^{noise}\|_{fro}$ is zero. In our setting, the error 336.6 implies the difference between initial and noised images. Note that "Barbara" image is comprised of 512×512 pixels, and each pixel belongs to $[0,1]$. We can observe that cartoon and texture are kept in Figure 1(c). However, there is noticeable blur at texture region in Figure 1(d).

3.2. Fractional Allen–Cahn Equation. It is known that the motion of interfaces for the classical Allen–Cahn equation follows the mean curvature flow [20]. In this section, we perform numerical simulations to compare the fractional and classical Allen–Cahn equations. Figure 2 shows the evolution of zero-contours of ϕ solving the fractional Allen–Cahn equation with different s values with circular and square initial conditions, respectively. Here, we used the following parameters: $N_x = 128$, $\Omega = (0,1)^2$, $\Delta t = 0.1$, the final time

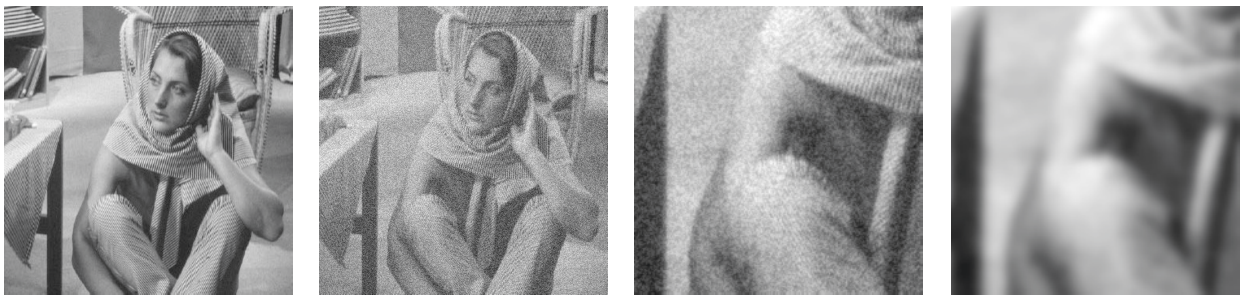

(a) (b) (c) (d)

FIGURE 1: (a) Original image f_0^{true}, (b) noise image f_0^{noise}, (c) close-up image at $\widetilde{\phi}^{0.5}$ with order $s = 0.5$, and (d) close-up image at $\widetilde{\phi}^{1}$ with order $s = 1.0$.

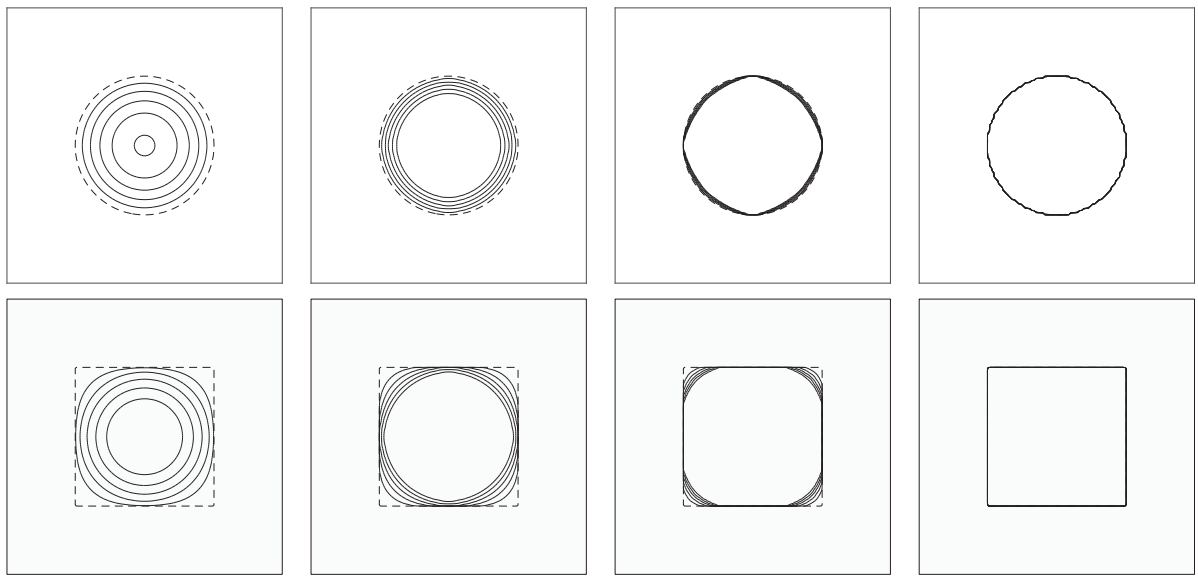

(a) $s = 1$ (b) $s = 0.5$ (c) $s = 0.25$ (d) $s = 0.1$

FIGURE 2: Evolution of zero-contours of ϕ solving fractional Allen–Cahn equation with different s values and circular (top) and square (bottom) initial conditions.

$T = 130$, $\epsilon = 0.0075$, and the dotted lines represent the initial conditions.

In Figure 2(a), the interfaces evolve as motions by mean curvature since it is the classical Allen–Cahn equation case, whereas we can observe that the dynamics is different from the classical one, especially at the tip of the interfaces, in Figures 2(b) and 2(c). When s is relatively small case, $s = 0.1$, the results give same shapes as the initial conditions (see Figure 2(d)). From the results, we can assume that it is better to capture a sharpen interface using the fractional Allen–Cahn equation with the proper s value and then using the classical Allen–Cahn equation.

3.3. Basic Figures. In this section, we consider the segmentation with basic figures. First, the segmentation results using classical and fractional Allen–Cahn equation with the following parameters are shown in Figure 3: $N_x = 256$, $\Omega = (0, 1)^2$, $\Delta t = 10$, $\epsilon = 0.01$, and $\mu = 10000$, and star-shaped initial condition. At the tip of the star, we can observe that the fractional Allen–Cahn equation gives better performance.

Next, we consider other segmenting simulations for two simple figures, circle and square, with salt and pepper noise using the following parameters: $N_x = 256$, $\Omega = (0, 1)^2$, $\Delta t = 10$, $\epsilon = 0.0038$ $\mu = 10000$. As shown in Figure 4, the case using the fractional Allen–Cahn equation (Figure 4(c)) gives better result than the case using classical Allen–Cahn equation (Figure 4(b)), especially at the corner of the square. However, the segmentation is interrupted by the noise when s becomes too small (see Figure 4(d)).

3.4. Medical Images. Here, we perform the numerical simulations applying the proposed segmentation algorithm to medical images. Figure 5 shows the segmentation results for brain CT image with and without injury [18] when (a) $s = 1$ and (b) $s = 0.05$ using the following parameters: $\Delta t = 10$, $\epsilon = 0.1$, and $\mu = 10000$. As opposed to the case with classical

(a) Initial (b) $s = 1$ (c) $s = 0.15$

Figure 3: (a) Initial condition and segmentation results with (b) classical and (c) fractional Allen–Cahn equations.

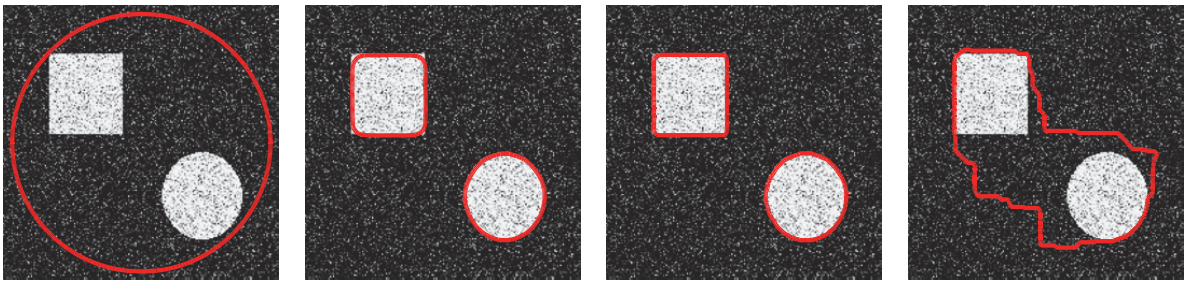

(a) Initial (b) $s = 1$ (c) $s = 0.25$ (d) $s = 0.15$

Figure 4: (a) Initial condition and (b)–(d) segmentation results with different s values.

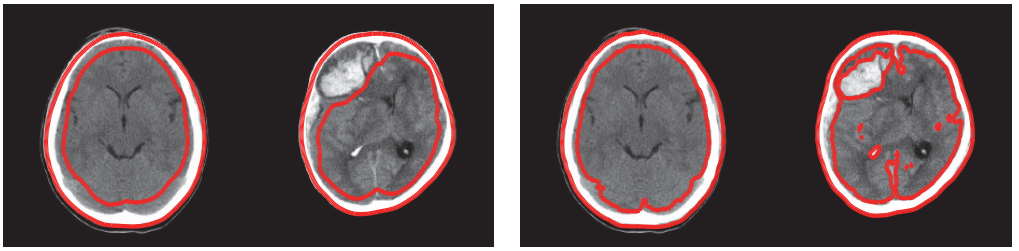

(a) $s = 1$ (b) $s = 0.05$

Figure 5: Segmentation results for brain CT images with (left) and without (right) injury [18] when (a) $s = 1$ and (b) $s = 0.05$.

Allen–Cahn equation, the injured part can be segmented in the case of Figure 5(b), which uses the fractional Laplacian operators.

4. Conclusions

We proposed the image segmentation model using the modified Allen–Cahn equation with a fractional Laplacian based on the Mumford–Shah energy functional. The fractional order, obtained as the macroscopic limit of Lévy process, was expected to change the dynamics of the Allen–Cahn equation. Based on the convex splitting method, we proved the unconditionally unique solvability and energy stability of the numerical scheme. The segmentation results show that the fractional Laplacian operator has a better performance when the original image has sharp tips and corners and the abnormalities are close to each other. Note that our approach requires parameter tuning for image segmentation. The best segmentation-parameter combination, including the fractional order "s", depends on the original image. The minimizer of our proposed functional is different for each of the initial images, so that we have to select the best parameter combination within all possible combinations of the parameters.

Data Availability

All the data used to support the findings of this study are available from the corresponding author upon request.

Conflicts of Interest

The authors declare that there are no conflicts of interest regarding the publication of this paper.

Acknowledgments

The author D. Lee was supported by the National Research Foundation of Korea (NRF) grant funded by the Korean Government (MSIP) (NRF-2015R1C1A1A01054694). The author S. Lee was supported by the National Institute for Mathematical Sciences (NIMS) grant funded by the Korean Government and the National Research Foundation of Korea (NRF) grant funded by the Korean Government (MSIP) (No. 2017R1C1B1001937).

References

[1] N. R. Pal and S. K. Pal, "A review on image segmentation techniques," *Pattern Recognition*, vol. 26, no. 9, pp. 1277–1294, 1993.

[2] N. Sharma, A. K. Ray, K. K. Shukla et al., "Automated medical image segmentation techniques," *Journal of Medical Physics*, vol. 35, no. 1, pp. 3–14, 2010.

[3] D. Mumford and J. Shah, "Optimal approximations by piecewise smooth functions and associated variational problems," *Communications on Pure and Applied Mathematics*, vol. 42, no. 5, pp. 577–685, 1989.

[4] L. Bar, T. F. Chan, G. Chung et al., "Mumford and Shah model and its applications to image segmentation and image restoration," *Handbook of Mathematical Methods in Imaging*, pp. 1–52, 2014.

[5] Y. Duan, H. Chang, W. Huang, J. Zhou, Z. Lu, and C. Wu, "The L_0 regularized Mumford-Shah model for bias correction and segmentation of medical images," *IEEE Transactions on Image Processing*, vol. 24, no. 11, pp. 3927–3938, 2015.

[6] S. Sashida, Y. Okabe, and H. K. Lee, "Application of Monte Carlo simulation with block-spin transformation based on the Mumford–Shah segmentation model to three-dimensional biomedical images," *Computer Vision and Image Understanding*, vol. 152, pp. 176–189, 2016.

[7] S. M. Allen and J. W. Cahn, "A microscopic theory for antiphase boundary motion and its application to antiphase domain coarsening," *Acta Metallurgica et Materialia*, vol. 27, no. 6, pp. 1085–1095, 1979.

[8] O. J. J. Algahtani, "Comparing the Atangana–Baleanu and Caputo–Fabrizio derivative with fractional order: Allen Cahn model," *Chaos, Solitons & Fractals*, vol. 89, pp. 552–559, 2016.

[9] Y. Nec, A. A. Nepomnyashchy, and A. A. Golovin, "Front-type solutions of fractional Allen-Cahn equation," *Physica D: Nonlinear Phenomena*, vol. 237, no. 24, pp. 3237–3251, 2008.

[10] S. Lee and D. Lee, "The fractional Allen-Cahn equation with the sextic GinzburgLandau potential," *Applied Mathematics and Computation*.

[11] R. Metzler and J. Klafter, "The random walk's guide to anomalous diffusion: a fractional dynamics approach," *Physics Reports*, vol. 339, no. 1, pp. 1–77, 2000.

[12] J. Bao, H. Wang, Y. Jia, and Y. Zhuo, "Cancellation phenomenon of barrier escape driven by a non-Gaussian noise," *Physical Review E: Statistical, Nonlinear, and Soft Matter Physics*, vol. 72, no. 5, Article ID 051105, 2005.

[13] A. V. Chechkin, V. Y. Gonchar, J. Klafter, and R. Metzler, "Barrier crossing of a Lévy flight," *EPL (Europhysics Letters)*, vol. 72, no. 3, pp. 348–354, 2005.

[14] A. V. Chechkin, O. Y. Sliusarenko, R. Metzler, and J. Klafter, "Barrier crossing driven by Lévy noise: Universality and the role of noise intensity," *Physical Review E: Statistical, Nonlinear, and Soft Matter Physics*, vol. 75, no. 4, Article ID 041101, 2007.

[15] P. D. Ditlevsen, "Anomalous jumping in a double-well potential," *Physical Review E: Statistical Physics, Plasmas, Fluids, and Related Interdisciplinary Topics*, vol. 60, no. 1, pp. 172–179, 1999.

[16] P. Imkeller and I. Pavlyukevich, "Lévy flights: transitions and meta-stability," *Journal of Physics A: Mathematical and General*, vol. 39, no. 15, pp. L237–L246, 2006.

[17] D. Jeong, S. Lee, D. Lee, J. Shin, and J. Kim, "Comparison study of numerical methods for solving the Allen-Cahn equation," *Computational Materials Science*, vol. 111, pp. 131–136, 2016.

[18] R. Liu, S. Li, C. L. Tan et al., "From hemorrhage to midline shift: A new method of tracing the deformed midline in traumatic brain injury CT images," in *Proceedings of the 2009 IEEE International Conference on Image Processing, ICIP 2009*, pp. 2637–2640, November 2009.

[19] M. Kwaśnicki, "Ten equivalent definitions of the fractional Laplace operator," *Fractional Calculus and Applied Analysis*, vol. 20, no. 1, pp. 7–51, 2017.

[20] D. S. Lee and J. S. Kim, "Mean curvature flow by the Allen-Cahn equation," *European Journal of Applied Mathematics*, vol. 26, no. 4, pp. 535–559, 2015.